Characteristic Analysis and Control Loop Design of Transmission Torque and Jerk for Flexible Joint Servo Systems

Can Wang, Yongquan Zhuang, Jinling Yang, Yuchao Liu, and Jianfei Pan, *Member, IEEE*

***Abstract*—In collaborative robot joint servo systems, harmonic reducers are mostly adopted as transmission devices, which helps to achieve light weight and flexibility. However, the introduction of a harmonic reducer or other transmission devices inevitably introduces elasticity into the system, resulting in mechanical oscillations and decreased joint output accuracy, which will reduce the safety and accuracy of the transmission system. This article investigates the dynamic characteristics of the transmission torque and jerk, which play a key role in the performance of servo transmission. The traditional servo control structure is then replaced by a novel control loop structure consisting of position, transmission torque and jerk. The parameters of the loop controllers are designed by means of the pole configuration method and an evaluation function. Finally, the accuracy and transmission safety of the designed control structure are verified by both simulation and experiment.**

***Index Terms*—Elastic servo system, transmission jerk, transmission safety, transmission torque.**

Nomenclature

T_e, T_s, T_L	Electromagnetic (motor) torque, transmission torque, load torque.
T_{sr}, T_{so}	Reference and observation of T_s.
$T_{sr\_\max}$, $T_{s\_\max}$	Maximum reference and limit of T_s.
$\dot{T}_s$	Transmission jerk.
$\dot{T}_{sr}$, $\dot{T}_{so}$	Reference and observation of $\dot{T}_s$.
$\dot{T}_{sr\_\max}$, $\dot{T}_{s\_\max}$	Maximum reference and limit of $\dot{T}_s$.
$T_s(0)$, $\dot{T}_s(0)$	Initial values of T_s and $\dot{T}_s$.
$T_{se}(0)$, $\dot{T}_{se}(0)$	Initial values of T_s and $\dot{T}_s$ under the action of T_e.
$T_{sL}(0)$, $\dot{T}_{sL}(0)$	Initial values of T_s and $\dot{T}_s$ under the action of T_L.
$\ddot{T}_s$, $\ddot{T}_{so}$	Transmission snap and its observation.
J_1, J_2	Motor inertia and load inertia.
K_s	Transmission stiffness coefficient.
θ_r, θ_m, θ_l	Reference, motor, and load position.
ω_m, ω_l	Motor speed, and load speed.
R	Ratio of J_2 to J_1.
ω_o	Oscillation frequency.
k_1, k_2	Coefficients of the state feedbacks.
F	Control gain of transmission jerk.
k_{pp}, k_{pd}	Proportional and differential coefficients of position loop controller.
P_1, P_2	Transfer functions of position controller and transmission torque controller.
ω_{pc}	Expected cut-off frequency.
φ_{pc}	Expected phase margin.

Manuscript received 27 November 2023; revised 13 February 2024; accepted 18 March 2024. Date of publication 27 March 2024; date of current version 16 May 2024. This work was supported in part by the National Natural Science Foundation of China under Grant 52007121, Grant 52277060, and Grant 52107084, and in part by General Research Project of Shenzhen Science and Technology Plan under Grant JCYJ20220818100000001 and Grant SGDX20230116110009018. Recommended for publication by Associate Editor J. Hur. *(Corresponding author: Jianfei Pan.)*

Can Wang, Yongquan Zhuang, Jinling Yang, and Jianfei Pan are with the College of Mechatronics and Control Engineering, Shenzhen University, Shenzhen 518061, China (e-mail: can.wang@szu.edu.cn; 2210295004@email.szu.edu.cn; 2070296038@email.szu.edu.cn; pjf@szu.edu.cn).

Yuchao Liu is with the Department of Mathematics, Physics, and Electrical Engineering, Northumbria University, NE1 8ST Newcastle Upon Tyne, U.K. (e-mail: yuchao.liu@northumbria.ac.uk).

Color versions of one or more figures in this article are available at https://doi.org/10.1109/TPEL.2024.3382006.

Digital Object Identifier 10.1109/TPEL.2024.3382006

I. Introduction

ROBOTS are widely used in industry and services [1], [2]. Most conventional robot joints use transmission mechanisms such as rotate vector reducers or gearboxes [3]. However, in order to achieve compactness, light weight, and flexibility, current robots commonly use harmonic reducers for transmission, which reduces the control accuracy [4]. Once the transmission torque exceeds the bearing range of the reducer, or the system works for a long time causing mechanical fatigue, it not only reduces the service life of the reducer, but also endanger the safety of the whole system [5].

In the joint servo system of a flexible robot, as shown in Fig. 1, the joint shaft is twisted and deformed due to the repeated high-speed deformation of the flexible wheel with the harmonic reducer, resulting in the transmission torque T_s (not the motor torque T_e) [6]. The unsafe factors of the system can be divided into three parts. Due to the easy installation of sensors or soft materials, the safety of the motor side and the load side can be easily guaranteed [7], [8], [9]. However, as an internal device, the limited bearing capacity and flexible connections of the reducer are prone to problems such as oscillations, shocks, or overload operation of the transmission torque and jerk, which are difficult to solve through mechanical or control strategies [10]. Therefore, the research on transmission safety poses a challenge for the optimization of robot servo systems [11].

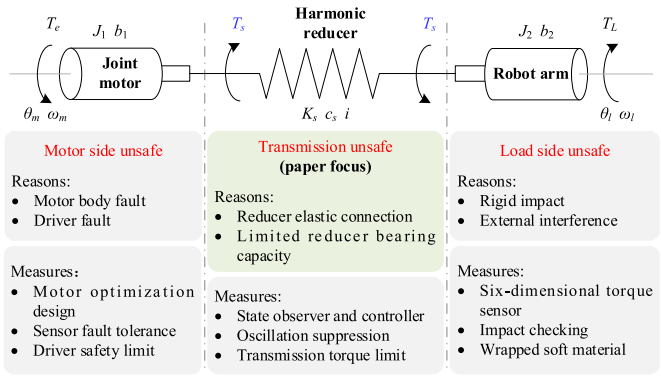

Fig. 1. Classification of unsafe factors and solutions of a joint servo system.

The essence of unsafe transmission of the flexible robot joint system lies in the elastic connection and the limited bearing capacity of the reducer. The former usually introduces mechanical oscillation into the system [12], while the latter usually brings poor performance during sudden torque changes [13]. In order to improve the transmission performance of the system and to provide theoretical guidance for the control method research, the transmission safety mechanism of the system should be elaborated.

Currently, most scholars have analyzed the mechanical oscillations caused by elastic connections such as limited stiffness, backlash, and friction [14], [15], [16]. However, few studies focus on the limited bearing capacity of reducers. The influence of dynamic load changes on shaft torsion is analyzed in a wind power transmission system in [17]. The reason for dynamic load limit of a horizontal flat rolling mill is studied in [18], and a fixed telemetry method is adopted to achieve continuous control of dynamic torque. In [19], torsional vibrations at nonzero frequencies in synchronous and asynchronous motor drive systems are analyzed, and it is shown experimentally that shaft torque limiting and line current harmonics can actually limit the losses at different operating frequencies of the motor.

To ensure the safety of servo systems, classical servo drivers are generally equipped with the ability to limit position, speed, and current by command constraints or controller output saturation [20]. However, as an internal state of the system, the transmission torque lacks an independent control loop for effective control and safe limitation.

The existing transmission state control methods include: state feedback control, model predictive control (MPC), and independent transmission state loop control [21], [22]. An improved disturbance observer is proposed in [23] to realize accurate contact force estimation using the joint torque sensor. In order to control the transmission torque directly, Serkies et al. [24] and Cychowski et al. [25] done a lot of work on MPC. In [25], the standard MPC controller is replaced by its explicit form. The resulting explicit controller achieves the same level of performance as the conventional MPC, but requires only a fraction of the real-time computing equipment, thus leading to fast and reliable implementation. An intelligent particle swarm optimization algorithm is employed in [26] to design the cost function of explicit MPC (EMPC), thus improving the search efficiency of the optimal coefficients. In combination with the direct torque control strategy, the application of a combined MPC to replace the position and speed loops can improve the field weakening performance of the system [27]. Although MPC provides a compact control design and ensures the system safety, the difficulty of parameter tuning and complex calculations makes its implementation in embedded drive system a challenge.

An effective solution to the above problem is closed-loop control of the transmission torque, but little research has been done in this area. In [28], a novel cascade methodology of forced dynamic control for the two-mass system is proposed. This method utilizes the pole configuration method to construct a shaft torque loop that acts as the inner loop of the speed control loop, which can effectively achieve shaft torque and speed tracking control. To reduce the effect of flexible loads on the wind turbine system, control loops for transmission torque and jerk are designed in [29] and [30]. To improve the speed tracking performance of the system, a speed outer loop is further designed. The existing loop control methods for transmission torque and jerk are mainly applicable to the inner loop of speed control. In contrast, there is a lack of research related to position control, which is of more concern for robotic joint systems.

Based on the above analysis, the characteristics of transmission torque and jerk are elaborated firstly in this article. Then, a novel servo cascade control structure consisting of position, transmission torque, and jerk is proposed. Considering that the robot joint system primarily focuses on position and torque control, and to reduce the complexity of the system design, this article omits the intermediate speed loop. Therefore, issues related to speed constraints need to be addressed in the position trajectory planning. Compared with the existing research, the main contributions of this article are as follows.

1) The operating characteristics of transmission torque and jerk in a flexible joint servo system are quantitatively analyzed for the first time.
2) The traditional servo control structure is replaced by a cascade loop of transmission torque, transmission jerk, and position. Based on the integral of time-weighted absolute error (ITAE) criterion and the frequency domain method, the controller parameters are designed to improve transmission accuracy and safety of the system.

The rest of this article is organized as follows. The flexible joint servo system is modeled in Section II. The analysis of the operation characteristics of the transmission torque and jerk are elaborated, taking into account the practical working conditions in Section III. In Section IV, the controllers of the three loops are designed. Experimental results are given in Section V. Finally, Section VI concludes this article.

II. Model of the Robot Joint Servo System

The dynamic model of the robot joint servo system is shown in Fig. 1. As an elastic transmission device, the reduction ratio of the reducer is i, the stiffness coefficient is K_s, and the damping coefficient is c_s. The electromagnetic torque T_e and transmission torque T_s act together on the motor (motor inertia is J_1 and damping coefficient is b_1), and T_e and T_s jointly determine the

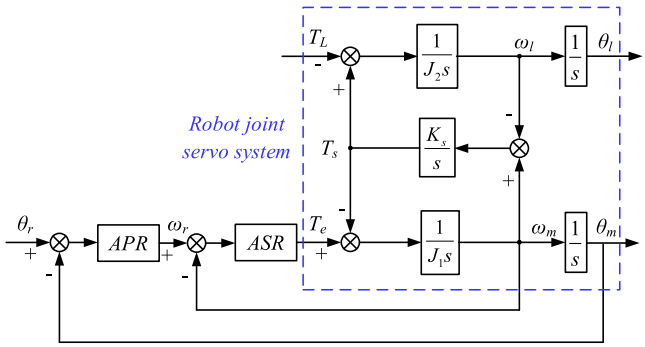

Fig. 2. Block diagram of the conventional servo control system.

motor position θ_m and speed ω_m. Meanwhile, T_s and load torque T_L work together on the robot arm and the load with load inertia of J_2 and load damping coefficient of b_2 to determine the load position θ_l and speed ω_l.

The impact of damping on the servo system is manifested as a resistive torque, which results from its product with the system speed. Therefore, it has a clear physical significance and can be analyzed separately. In addition, to simplify the design process of the control method and considering the feasibility of implementing the transmission torque state-space modeling, damping is neglected in the system model in this article. Then, the state equation of the system motion can be established as shown in (1), where the state is chosen as $x(t) = [\omega_m\, \omega_l\, T_s\, T_L]^T$, the input $u(t) = T_e$, and the output $y(t) = \omega_m$

$$\begin{cases} \dot{x}(t) = Ax(t) + Bu(t) \\ y(t) = Cx(t) \end{cases} \tag{1}$$

$$A = \begin{bmatrix} 0 & 0 & -1/J_1 & 0 \\ 0 & 0 & 1/J_2 & -1/J_2 \\ K_s & -K_s & 0 & 0 \\ 0 & 0 & 0 & 0 \end{bmatrix},$$

$$B = \begin{bmatrix} 1/J_1 \\ 0 \\ 0 \\ 0 \end{bmatrix}, C = \begin{bmatrix} 1 \\ 0 \\ 0 \\ 0 \end{bmatrix}^T.$$

Most conventional servo control structures consist of position and speed loops, where the electromagnetic torque loop is simplified due to its fast response, and the block diagram is shown in Fig. 2. *APR* and *ASR* denote position regulator and speed regulator, respectively, and they are mostly implemented by proportion-integral-derivative controllers. The blue dashed box indicates the mechanical structure of the system, which corresponds to (1).

The transfer functions from T_e to T_s and from T_L to T_s are, respectively, as follows:

$$\frac{T_s(s)}{T_e(s)} = \frac{J_2K_s}{J_1J_2s^2 + (J_1K_s + J_2K_s)} \tag{2}$$

$$\frac{T_s(s)}{T_L(s)} = \frac{J_1K_s}{J_1J_2s^2 + (J_1K_s + J_2K_s)}. \tag{3}$$

From (2) and (3), the oscillation frequency ω_o can be deduced as in (4), where ω_o is related to the stiffness of the transmission device

$$\omega_o = \sqrt{\frac{(J_1 + J_2)K_s}{J_1J_2}}. \tag{4}$$

According to the superposition theorem, the frequency domain expression for T_s is

$$T_s(s) = \frac{K_s\left[J_2T_e\left(s\right) + J_1T_L\left(s\right)\right]}{J_1J_2s^2 + (J_1K_s + J_2K_s)}. \tag{5}$$

III. Characteristics of the Transmission States

A. Transmission Torque

According to (1), we can obtain a second-order differential equation for $T_s(t)$, expressed as follows:

$$\ddot{T}_s\left(t\right) = K_s \cdot \left(\frac{T_e(t) - T_s(t)}{J_1} - \frac{T_s(t) - T_L(t)}{J_2}\right). \tag{6}$$

Furthermore, by using (4), we can rearrange (6) as follows:

$$\ddot{T}_s\left(t\right) + \omega_o^2 \cdot T_s(t) - \frac{K_s}{J_1} \cdot T_e(t) - \frac{K_s}{J_2} \cdot T_L(t) = 0. \tag{7}$$

Under common operating conditions of robot joint systems, such as motor start-up, steady state, and external disturbances, the effect of T_e and T_L on the system can always be simulated by step signals. Thus, there are $L\{T_e(t)\} = \frac{T_e}{s}$ and $L\{T_L(t)\} = \frac{T_L}{s}$, where T_e and T_L are the values of the two variables, respectively.

To comprehensively study the system's response induced by nonzero excitation and initial conditions, the Laplace transform is used. The results when T_e and T_L act separately are expressed as (8) and (9), respectively, where $T_{se}(0)$ and $\dot{T}_{se}(0)$ represent the initial values of T_s and $\dot{T}_s$ under the action of T_e, while $T_{sL}(0)$ and $\dot{T}_{sL}(0)$ represent the initial values of T_s and $\dot{T}_s$ under the action of T_L

$$s^2 \cdot T_s(s) + s \cdot T_{se}\left(0\right) + \dot{T}_{se}\left(0\right) + \omega_o^2 \cdot T_s(s) - \frac{K_sT_e}{J_1s} = 0 \tag{8}$$

$$s^2 \cdot T_s(s) + s \cdot T_{sL}\left(0\right) + \dot{T}_{sL}\left(0\right) + \omega_o^2 \cdot T_s(s) - \frac{K_sT_L}{J_2s} = 0. \tag{9}$$

Furthermore, by performing the inverse Laplace transform on (8) and (9), we can obtain the time-domain expressions of T_s when T_e and T_L act separately. According to the superposition theorem, the time-domain expression of $T_s(t)$ can be obtained when T_e and T_L act together, as shown in (10). In this expression, the system inertia ratio is denoted as $R = J_2/J_1$, which is the system's inertia ratio, and the initial value of T_s and $\dot{T}_s$ after merging is $T_s(0) = T_{se}(0) + T_{sL}(0)$ and $\dot{T}_s(0) = \dot{T}_{se}(0) + \dot{T}_{sL}(0)$, respectively, as follows:

$$T_s\left(t\right) = \underbrace{\frac{RT_e + T_L}{1 + R}\left[1 - \cos\left(\omega_o t\right)\right]}_{\text{zero state response}}$$

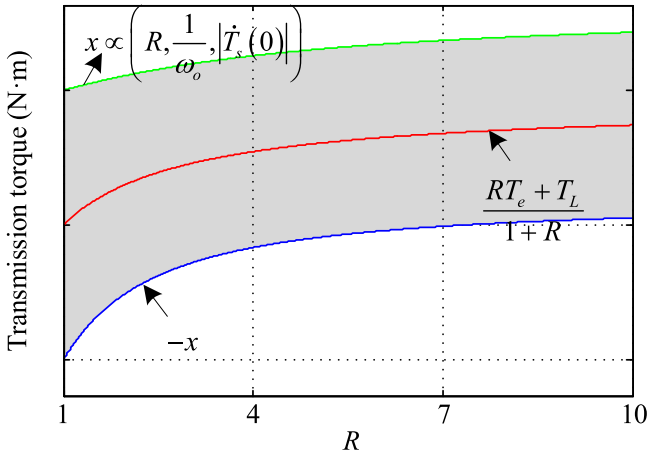

Fig. 3. Schematic diagram of the dynamic oscillation of T_s.

$$+ \underbrace{\left[T_s(0)\cos(\omega_o t) + \frac{\dot{T}_s(0)}{\omega_o}\sin(\omega_o t)\right]}_{\text{zero input response}}. \quad (10)$$

Using trigonometric function relationships, we can simplify (10) as

$$T_s(t) = \frac{RT_e + T_L}{1+R} + x \cdot \sin(\omega_o t + y) \quad (11)$$

$$\text{where } \begin{cases} x = \sqrt{\left[T_s(0) - \frac{RT_e+T_L}{1+R}\right]^2 + \left(\frac{\dot{T}_s(0)}{\omega_o}\right)^2} \\ y = \arctan\left[\frac{\omega_o}{\dot{T}_s(0)}\left(T_s(0) - \frac{RT_e+T_L}{1+R}\right)\right] \end{cases}.$$

From (11), T_s is an oscillatory signal with an oscillation frequency of ω_o, an amplitude of x, and an offset of $\frac{RT_e+T_L}{1+R}$. Considering the load inertia, the maximum speed of the motor, and the mechanical space limitation, R is usually configured in the range of 1 to 10. According to (11), when both T_e and T_L are constants, Fig. 3 illustrates a schematic representation of the response of T_s. It can be seen that the oscillation amplitude $|x|$ is positively correlated with R and $|\dot{T}_s(0)|$, and inversely correlated with ω_o. It is worth noting that Ts will exhibit damped oscillations if the damping of the system is taken into account.

B. Transmission Jerk

Sudden disturbances often lead to drastic changes in the system states, exacerbating the transmission unsafety, so the dynamic characteristics of the transmission jerk $\dot{T}_s$ should also be analyzed. According to (11), the time-domain expression of $\dot{T}_s$ shown in (12) can be derived

$$\dot{T}_s(t) = \omega_o x \cdot \cos(\omega_o t + y). \quad (12)$$

For an actual flexible robot joint system, the transmission devices usually include reducers, shafts, and couplings. The specific oscillation frequency distribution is about 30 to 300 Hz. According to (12), a schematic diagram of the dynamic response of $\dot{T}_s$ is shown in Fig. 4, where the oscillation amplitude is $\omega_o x$. Unlike T_s, the amplitude of $\dot{T}_s$ is positively correlated with ω_o. Once the bearing capacity of the transmission device is exceeded, the safety of the entire servo system will be compromised.

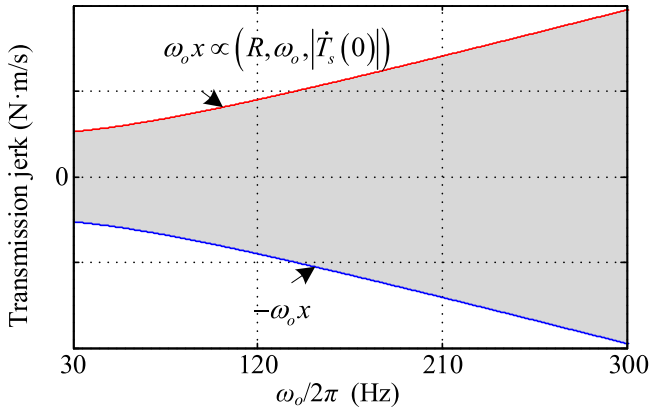

Fig. 4. Schematic diagram of the dynamic oscillation of $\dot{T}_s$.

C. Common Working Conditions Discussion

Since dramatic changes in T_s and $\dot{T}_s$ will be caused by motor start-up or sudden disturbances, both cases are discussed below.

1) Motor Start-Up: When the motor is accelerated from standstill, $T_s(0) = \dot{T}_s(0) = 0$. According to (11), the maximum steady-state value of T_s can be obtained, as shown in (13). On the other hand, the corresponding maximum value of $\dot{T}_s$ can be derived, as expressed in (14)

$$T_{s\_\max 1} = 2\left|\frac{RT_e + T_L}{1+R}\right| \quad (13)$$

$$\dot{T}_{s\_\max 1} = \left|\frac{(RT_e + T_L)\omega_o}{R+1}\right|. \quad (14)$$

It can be seen that $T_{s\_\max 1}$ is related to the instantaneous values of T_e and T_L as the motor is started. As R increases, the fluctuation range expands. Whereas, $\dot{T}_{s\_\max 1}$ is related to not only the above factors but also ω_o.

2) Sudden Disturbance: Due to the random nature of sudden loads, the instantaneous value of T_s is inevitably related to the initial conditions, i.e., $T_s(0)$ and $\dot{T}_s(0) \neq 0$. According to (11), when a sudden load occurs, the maximum value of T_s can be derived as (15). Similarly, the maximum value of $\dot{T}_s$ can be deduced as (16). It can be seen that both $T_{s\_\max 2}$ and $\dot{T}_{s\_\max 2}$ are related to $T_s(0)$ and $\dot{T}_s(0)$. Different loading times result in significant differences in $T_s(0)$ and $\dot{T}_s(0)$

$$T_{s\_\max 2} = \left|\frac{RT_e + T_L}{1+R}\right| + x \quad (15)$$

$$\dot{T}_{s\_\max 2} = \omega_o x. \quad (16)$$

The properties of T_s and $\dot{T}_s$ can guide not only the design of saturation values, but also the selection of system components.

IV. Limiting Control Based on Transmission States Cascade Loops

From the analysis above, the time-domain responses of T_s and $\dot{T}_s$ are both oscillating signals, which seriously affect the

TABLE I
MAIN PARAMETERS OF THE FLEXIBLE TRANSMISSION SERVO SYSTEM

Parameter	Nominal value
Motor power	1 kW
Rated torque	4.77 N·m
Rated speed	2000 r/min
Rated current	5.2 A
Motor inertia	$6.18*10^{-4}$ kg·m^2
Load inertia	$22.9*10^{-4}$ kg·m^2
Flywheel	$30.9*10^{-4}$ kg·m^2
Transmission stiffness	380 N·m/rad
Encoder resolution	23 bit

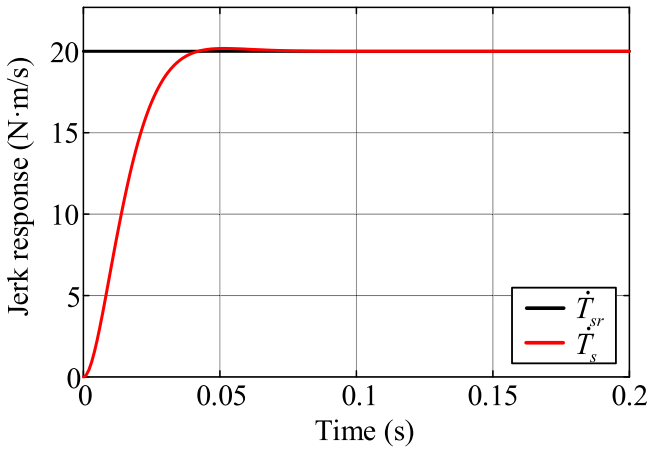

Fig. 5. Step response of the transmission jerk loop.

transmission performance of the system and even endanger the safety of the entire system. Since the traditional servo system lack a specific loop control for the transmission states, it cannot solve the transmission problem. Therefore, a cascade control loop of T_s and $\dot{T}_s$ is established in this article.

A. State Space Model of Transmission Jerk

The state space model consisting of T_s and $\dot{T}_s$ has zeros at the origin of the complex plane, making the system unstable. Therefore, the state matrix is constructed of $\dot{T}_s$ and $\ddot{T}_s$. According to (1), the state space can be established to be represented in

$$\begin{bmatrix} \ddot{T}_s \\ \dddot{T}_s \end{bmatrix} = \begin{bmatrix} 0 & 1 \\ -\frac{K_s}{J_1} - \frac{K_s}{J_2} & 0 \end{bmatrix} \begin{bmatrix} \dot{T}_s \\ \ddot{T}_s \end{bmatrix} + \begin{bmatrix} 0 \\ \frac{K_s}{J_1} \end{bmatrix} \dot{T}_e + \begin{bmatrix} 0 \\ \frac{K_s}{J_2} \end{bmatrix} \dot{T}_L \tag{17}$$

$$\dot{T}_s = \begin{bmatrix} 1 & 0 \end{bmatrix} \begin{bmatrix} \dot{T}_s \\ \ddot{T}_s \end{bmatrix}. \tag{18}$$

The input equation is (19), where k_1 and k_2 are the parameters of the state controller and F is a control gain

$$\dot{T}_e = \begin{bmatrix} k_1 & k_2 \end{bmatrix} \begin{bmatrix} \dot{T}_s \\ \ddot{T}_s \end{bmatrix} + F\dot{T}_{sr}. \tag{19}$$

In order to verify the performance of the designed control structure, a simulation model is built with the parameters shown in Table I. In Fig. 5, the step response of $\dot{T}_s$ loop at 20 N·m/s is tested. It is clear that the reference transmission jerk $\dot{T}_{sr}$ can be tracked within 0.05 s, which proves the good tracking performance.

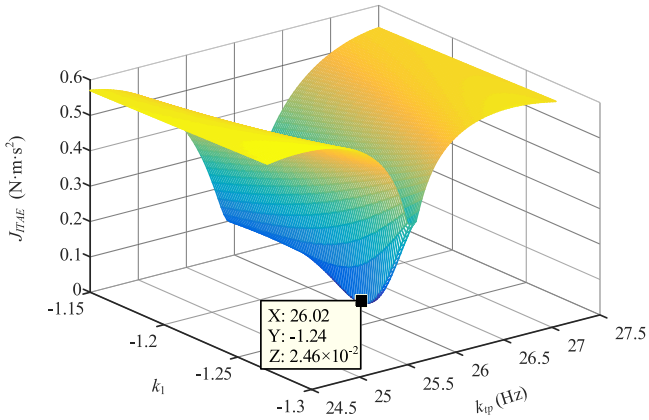

Fig. 6. Three-dimensional relationship diagram of J_{ITAE}, k_{tp}, and k_1.

B. Control Loop Design of Transmission Torque

In addition to $\dot{T}_s$ loop, a T_s loop is added, and a proportional controller (P) with a coefficient of k_{tp} is selected.

In order to balance the rapidity and accuracy of the response of T_s, an evaluation function J_{ITAE} based on the time integral of the absolute value of $e(t) = T_{sr}(t)$ - $T_s(t)$ is established in (20), where T_{sr} and T_s are the reference transmission torque and the actual transmission torque, respectively, and k_1, k_2, and k_{tp} are the parameters to be designed. When J_{ITAE} reaches the minimum value, the tracking error is guaranteed to be minimal and therefore the local optimal tracking performance of T_s is achieved

$$J_{\mathrm{ITAE}} = \int_0^t t\,|e(t)|dt = \int_0^t t\,|T_{sr}(t) - T_s(t)|dt. \tag{20}$$

Since k_2 is the feedback coefficient of $\ddot{T}_s$, the smaller k_2 is, the better the smoothness of the compensation. After repeated tests, k_2 is set to be 0.0003. Thus, a three-dimensional relationship diagram between J_{ITAE}, k_{tp}, and k_1 is depicted in Fig. 6. Obviously, the minimum value of J_{ITAE} is 2.46×10^{-2} N·m·s^2, i.e., the best tracking performance can be obtained when $k_{tp} =$ 26.02 Hz and $k_1 = -1.24$.

To verify the performance of T_s loop, a step signal of half the rated torque (2.385 N·m) is given, and the saturation values of T_e and $\dot{T}_s$ are set to the motor rated torque and 20 N·m/s, respectively. The simulation results are given in Fig. 7. It can be seen that T_s can keep stable within 0.2 s without tracking error, which indicates its good dynamic performance. The steady-state value of T_e is about 3 N·m, which provides power to both the drive and load sides together. From Fig. 7(b), $\dot{T}_s$ can be well stabilized at the set saturation value, which is also consistent with the slope of T_s shown in Fig. 7(a).

C. Control Loop Design of the Position

In order to meet the positioning requirements of the robot joint, a position loop should be added. A proportional derivative

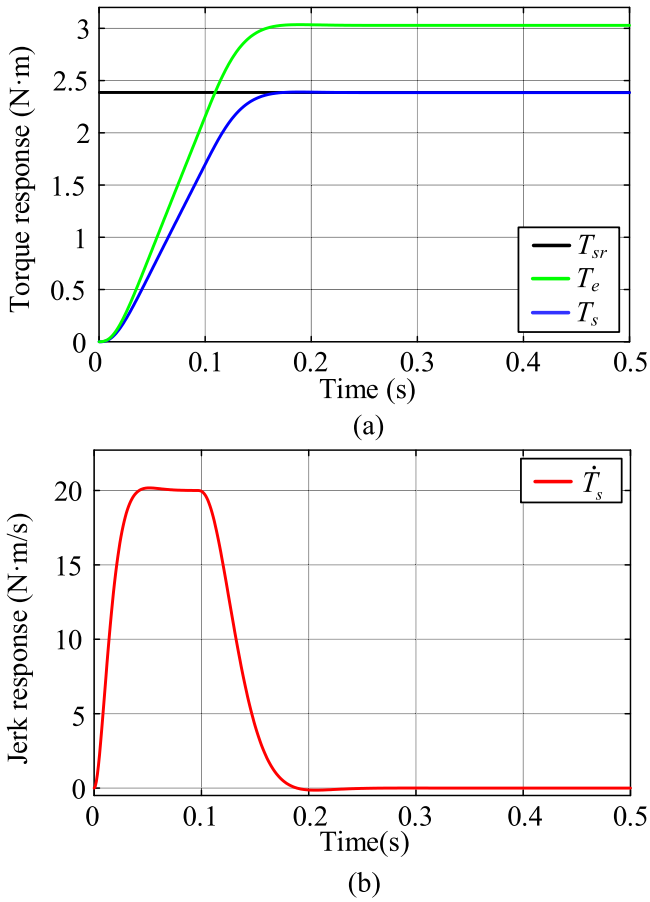

Fig. 7. Step responses of the transmission torque loop.

(PD) controller is chosen with the proportional and differential coefficients k_{pp} and k_{pd}, respectively. The role of the derivative term is equivalent to indirectly controlling the motor's speed.

The open-loop transfer function from the reference position θ_r to the actual motor position θ_m is shown in (21), where P_1 and P_2 are the transfer functions of the PD controller in the position loop shown in (22) and the P controller in the transmission torque loop shown in (23), respectively, as follows:

$$G_p(s) = \frac{\theta_m}{\theta_r} = \frac{FJ_2P_1P_2s^2 + FP_1P_2K_s}{J_1J_2s^5 + J_2k_2K_ss^4 + (J_1K_s + J_2K_s + J_2k_1K_s)s^3 + FJ_2K_sP_2s^2} \tag{21}$$

$$P_1 = k_{pp} + k_{pd}s \tag{22}$$

$$P_2 = k_{tp}. \tag{23}$$

Considering the expected cut-off frequency ω_{pc} and phase margin φ_{pc} in (24), the parameters of the PD controller are designed by the frequency domain approach. According to Section IV-B, the ω_{pc} and of T_s loop can be calculated as 25 rad/s and 67.9°, respectively. Since the position loop is served as an outer loop, the cut-off frequency should be less than that of T_s loop.

Moreover, there has to be a tradeoff between transmission tracking and fast positioning. Accordingly, the desired cut-off frequency of the position loop ω_{pc} is set to be 0.2 times the transmission torque loop, i.e., 5 rad/s, while φ_{pc} is designed to be 57°. Then, $k_{pp} = 0.02$ and $k_{pd} = 0.01$ can be obtained from

$$\begin{cases} |G_p(j\omega_{pc})| = 1 \\ \angle G_p(j\omega_{pc}) = \varphi_{pc} - \pi. \end{cases} \tag{24}$$

D. Saturation Design of Transmission Torque and Jerk

For the control loops of T_s and $\dot{T}_s$, it is necessary to design the respective saturation values with reference to the following three aspects.

1) User requirements.
2) The maximum mechanical torque and instantaneous impulse that the transmission mechanism can withstand for long-term operation.
3) Practical applications and working conditions.

The following 1) and 2) are based on the specific requirements of the user or are related to the transmission equipment selected for the joint system and therefore are not analyzed. For 3), the idea of designing saturation values for T_s and $\dot{T}_s$ can follow the conclusions of the characteristic analysis of both in Section III. That is, $T_{sr\_\max}$ should satisfy both (13) and (15), as shown in (25), while $\dot{T}_{sr\_\max}$ should satisfy both (14) and (16), as shown in (26)

$$T_{sr\_\max} < \min\{T_{s\_\max 1}, T_{s\_\max 2}\} \tag{25}$$

$$\dot{T}_{sr\_\max} < \min\left\{\dot{T}_{s\_\max 1}, \dot{T}_{s\_\max 2}\right\}. \tag{26}$$

E. Observer Design

In this article, a Luenberger state observer is chosen to implement the state feedback [31], and its recursive equation is shown in (27). The state matrix is $\hat{x} = [\hat{\omega}_m \quad \hat{\omega}_l \quad \hat{T}_s \quad \hat{T}_L]^T$, the feedback matrix is $L = [l_1\ l_2\ l_3\ l_4]^T$, and the system, input, and output matrices are as expressed in (1)

$$\dot{\hat{x}} = (A - LC)\hat{x} + Bu + Ly. \tag{27}$$

In order to apply the observer to a practical system, the exact discretization method is applied. The obtained discrete state equation is shown in (28), where T is the sampling time

$$\begin{cases} \hat{x}(k+1) = G\hat{x}(k) + Hu(k) \\ y(k) = C\hat{x}(k) \end{cases}$$

$$G = e^{AT}H = \int_0^T e^{AT}Bdt. \tag{28}$$

The Gramian of this observation system is shown in (29). Since it is nonsingular, the system is fully observable

$$Q_0 = \begin{bmatrix} C_o & C_oG & C_oG^2 & C_oG^3 \end{bmatrix}^T = 4. \tag{29}$$

The characteristic equation of the observer is given by

$$a(z) = |zI - (G - LC_o)|. \tag{30}$$

The performance of the observer is typically characterized by two aspects: when the observer poles are closer to 0, the

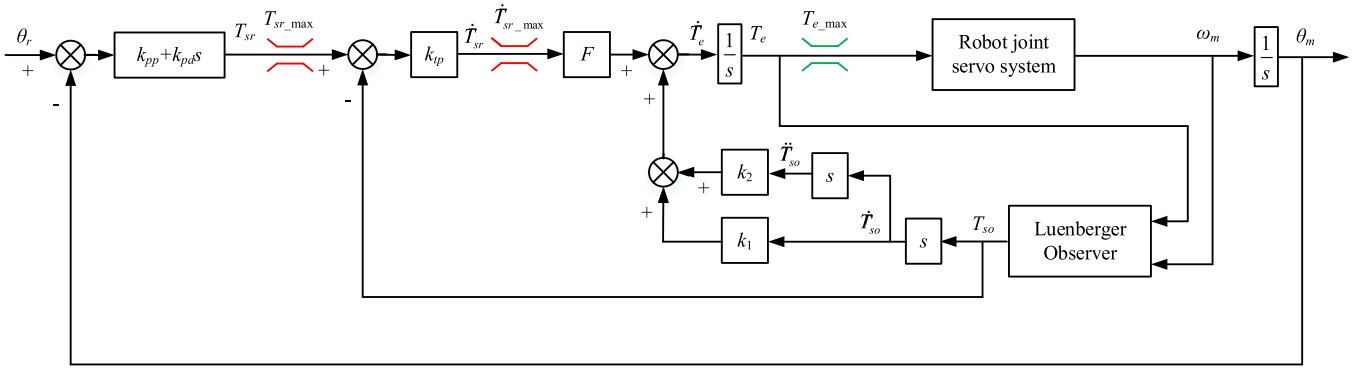

Fig. 8. Block diagram of the complete three control loops of position, transmission torque, and transmission jerk.

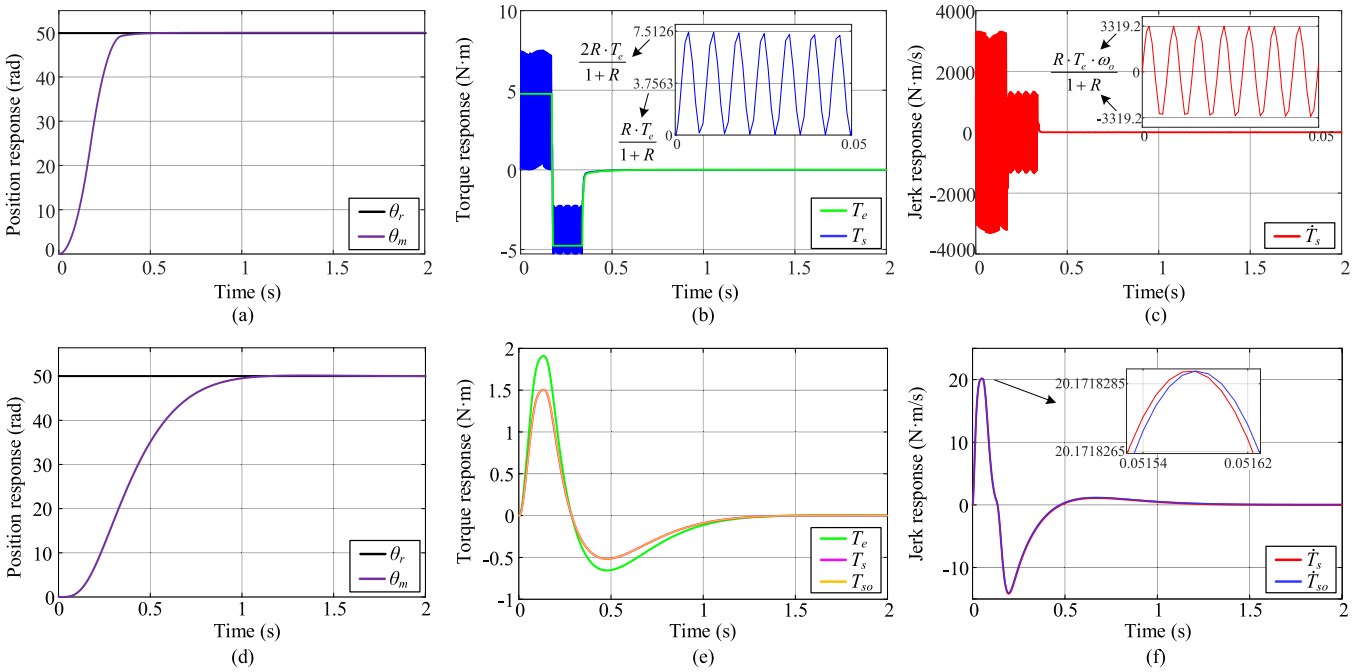

Fig. 9. Simulation comparison results. (a)–(c) Traditional servo control structure shown in Fig. 2. (d)–(f) Proposed control structure shown in Fig. 8.

observation speed is faster, but the observation noise is greater; conversely, when the observer poles are closer to 1, the observation speed is slower, but the observed results are smoother. Since the transmission torque control studied in this article is generally applied in scenarios where precise and smooth torque tracking is more critical than high response speed, a balance between observation noise and observation speed is considered. Therefore, all four poles of the observer are configured to be 0.8, as shown in (31). This choice makes them closer to 1, resulting in smoother observation results. From this configuration, the feedback matrix L can be derived

$$\alpha^*(z) = (z-0.8)^4. \tag{31}$$

F. Complete Control Block and Simulation Results

Finally, the block diagram of the proposed servo control structure consisting of position, transmission torque and jerk is obtained, as shown in Fig. 8. To validate the performance of the servo control structure designed in this article, Fig. 9 compares the performance of the conventional servo control structure at a 50 rad step reference position. In the conventional servo control structure, the *APR* and *ASR* adopt common P and PI regulators, respectively, following typical servo tuning methods [32].

From Fig. 9(a)–(c), it can be observed that typical servo tuning methods result in a fast position response, with T_e quickly reaching saturation. However, during the acceleration phase, T_s and $\dot{T}_s$ show continuous oscillations. The apparent oscillations come from the large controller stiffness set by conventional servo structures to ensure fast tracking. The oscillation characteristics of T_s and $\dot{T}_s$ are further verified by the local magnification plots from 0 to 0.05 s given in Fig. 9(b) and (c). The median and amplitude of the oscillations are in perfect agreement with the numerical solution of (11) and (12). Moreover, when T_e reaches negative saturation (about 0.2–0.3 s), the amplitudes of transmission torque and its jerk are smaller than when T_e reaches positive saturation (about 0–0.2 s). This is due to the fact that

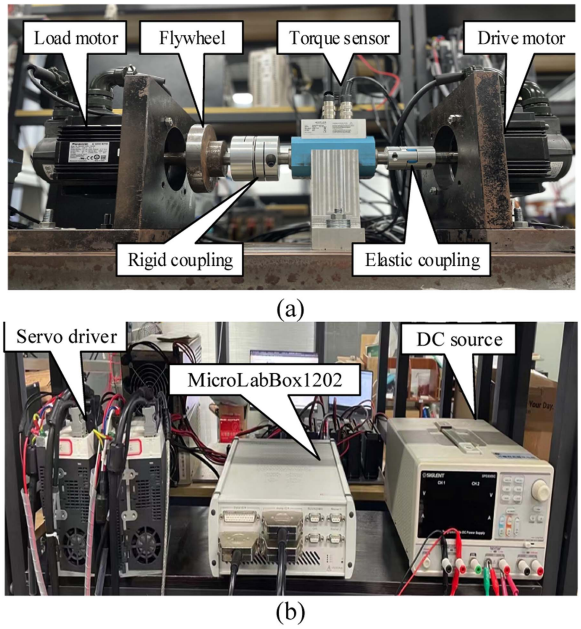

Fig. 10. Picture of the experimental setup (a) mechanical part (b) control part.

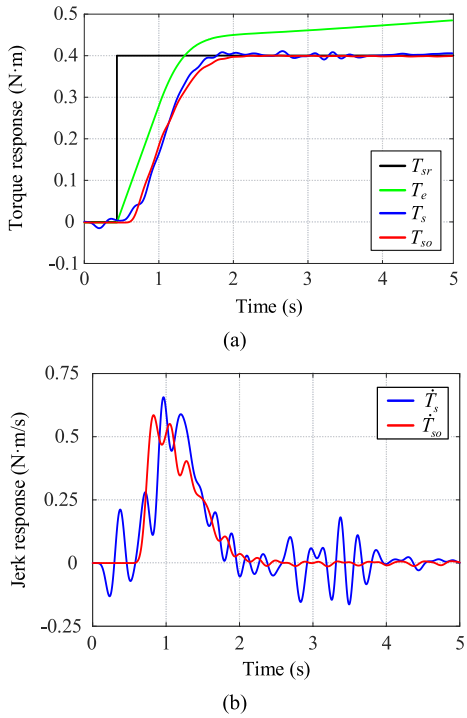

Fig. 11. Step response of transmission torque loop.

the initial values $T_{se}(0)$ and $\dot{T}_{se}(0)$ are no longer zero, which is consistent with the theoretical analysis in Section III.

Fig. 9(d)–(f) shows the results of the proposed servo control structure, where T_s is limited to 1.5 N·m and other conditions are consistent with the previous ones. It can be seen that the position tracking is slower than the conventional servo control structure. However, neither T_e nor T_s exceeds the saturation value, and T_s is roughly 0.8 times of T_e, which is consistent with the theoretical analysis. $\dot{T}_s$ remains within the saturation value when T_s increases or decreases. When the motor reaches a given position, all the torques in the system are balanced, and $\dot{T}_s$ is 0. In addition, the observer results are displayed in Fig. 9(e) and (f), where the subscript "o" indicates the observed values. Clearly, T_{so} closely matches the actual value T_s. $\dot{T}_{so}$ lags slightly behind $\dot{T}_s$, with a time delay on the level of microseconds.

It can be seen that the conventional servo control structure cannot control the transmission characteristics of the system. The servo control structure investigated in this article allows for effective limiting and precise tracking control of the transmission torque and jerk. Although this inevitably involves some loss of tracking speed, it is suitable for robotic systems concerned with torque flexibility and precise control.

V. Experiment Results

A. Experimental Setup

The experiment setup of the flexible transmission servo system is constructed in Fig. 10. For the mechanical part shown in Fig. 10(a), both the drive motor and the load motor are Panasonic© MINAS A6 series permanent magnet synchronous motors (PMSM). The output electromagnetic torque T_e is sent to the motor driver as the reference signal of the torque loop through the digital to analog converter (DAC) and analog to digital converter (ADC) modules. The load motor acts as a generator to provide the load torque T_L, which is transmitted to the load driver for loading the system. Both the servo drivers are set to torque loop control mode to receive torque commands T_e and T_L, and control the motor motion by field-oriented control technique. The actual motor position is measured by an absolute encoder and the motor speed is obtained by the speed calculation module of dSPACE for the implementation of the Luenberger observer. The motor speed is planned by the slope of the reference position. An elastic NBK coupling is used to simulate flexible transmission mechanisms such as reducers. The measured transmission torque is obtained by a KISTLER torque sensor with a low-pass filter, while its first-order differential is considered as the measured transmission jerk. The observed values of transmission torque differentiations for state feedback undergo the same filtering process. The flywheel is removable for simulating different load inertia situations.

Experiments are constructed on MATLAB/Simulink and compiled and executed on dSPACE MicroLabBox1202. The specific platform parameters are shown in Table I. Considering the tradeoff between the control system's requirements for flexibility and rapidity in this study, the sampling time is set to 1 ms.

B. Response of Transmission Torque Loop

To verify the inner-loop performance of transmission torque and jerk and to ensure system safety, a step T_{sr} of 0.4 N·m is given. The saturation values of $\dot{T}_s$ and T_e are set to be ± 0.5 N·m/s and the motor rated torque, respectively. The system response is shown in Fig. 11, where the subscripts o and r stand for the observed and the reference values, respectively.

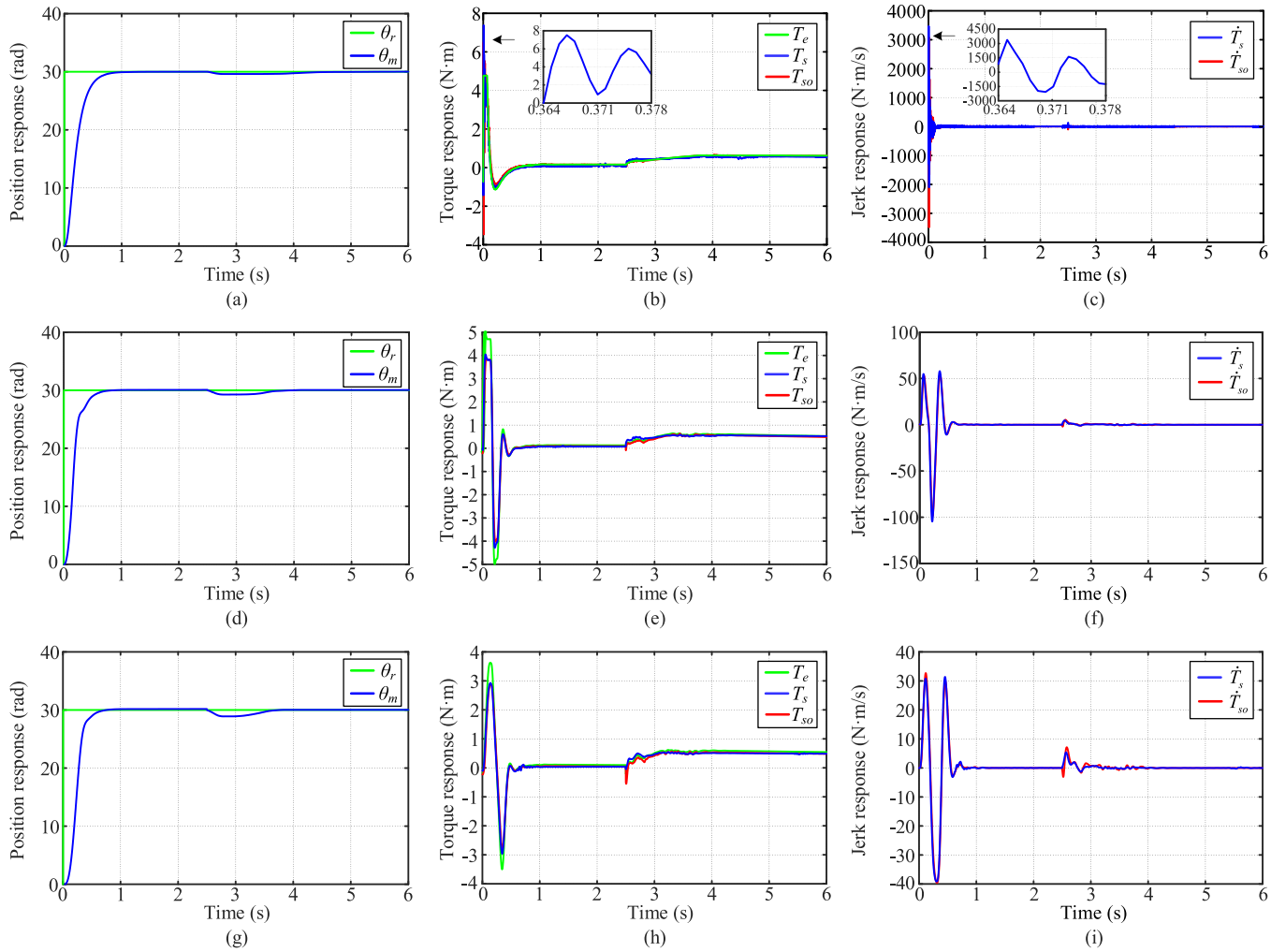

Fig. 12. Experimental comparison results at $T_L = 0.477$ N·m. (a)–(c) Conventional servo control structure (d)–(f) proposed control structure without and (g)–(i) with ±3 N·m transmission torque and ±40 N·m/s transmission jerk saturation values.

As can be seen in Fig. 11(a), the measured T_s almost matches the observed T_{so} and track T_{sr} after about 1.5 s without overshoot. Since $\dot{T}_{sr\_\max}$ is designed to be small, the response of T_s is not very fast. T_e is faster and its amplitude is larger than T_s, as it needs to drive both the motor and the load. Furthermore, the constant T_{sr} keeps the system in continuous acceleration, in which case, the product of speed and damping results in a torque added to T_e. It leads to a slight upward trend of T_e after 2 s. After the first-order differential process, the measured $\dot{T}_s$ and the observed $\dot{T}_{so}$ are shown in Fig. 11(b), in which the same trend can be seen. During the acceleration phase of the system, the two states oscillate slightly around the saturation value of 0.5 N·m/s. When T_s has tracked the reference value, both states drop to zero.

C. Response of the Proposed Servo Control Structure

Fig. 12 shows the experimental results of the conventional servo structure and the proposed servo control structure at a reference position of 30 rad, an electromagnetic torque limit of one times the rated torque, and a sudden load of 10% of the rated torque at 2.5 s.

As a comparison, the performance of the conventional servo control structure consisting of position and speed is shown in Fig. 12(a)–(c). By reducing the stiffness of the controllers, the position response can be slowed down, thereby alleviating oscillations in T_s and $\dot{T}_s$. Therefore, in the traditional servo control structure, the stiffness of *APR* and *ASR* is reduced to roughly align with the position tracking time of the proposed servo control structure. This is done for better comparison of the performance differences between the two in torque response.

As can be seen, the torques increase immediately to accommodate the fast position response. From Fig. 12(a), the slope of the motor position is large in 0–0.2 s, which means that the motor speed reaches its maximum value and the corresponding electromagnetic torque reaches its saturation value and remains for 0.2 s, as shown in Fig. 12(b). The decrease in the motor position slope over 0.2–0.8 s indicates a gradual decrease in motor speed to zero, which should theoretically correspond to a negative value of the electromagnetic torque. The presence of system damping makes the final steady-state value of the electromagnetic torque slightly greater than zero. Therefore, while it is possible to alleviate the oscillations in T_s and $\dot{T}_s$

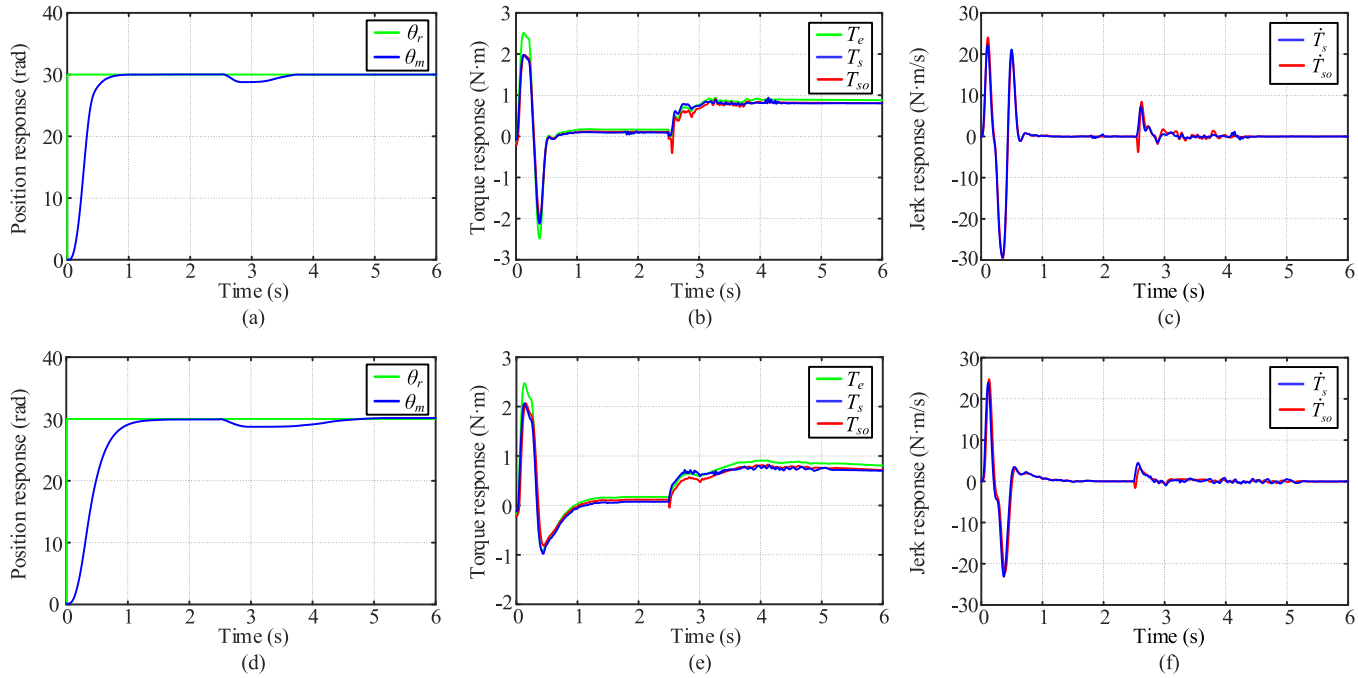

Fig. 13. Experimental results for the proposed control structure at $T_L = 0.7155$ N·m. (a)–(c) $J_2 = 22.9\times10^{-4}$ kg·m^2 (d)–(f) $J_2 = 53.8\times10^{-4}$ kg·m^2.

by slowing down the position response, it still cannot achieve precise tracking control of the two.

The results shown in Fig. 12(a)–(c) also verify the characteristics of the transmission states presented in Section III. According to (4), the oscillation frequency of the system is 140 Hz, and the amplitude of T_e is 4.77 N·m. Therefore, according to Section III-A, T_s should theoretically oscillate with a median value of 3.76 N·m, a range of 0 to 7.52 N·m, and a frequency of 140 Hz (period is about 0.007 s). In addition, according to (12), the amplitude and oscillation frequency of $\dot{T}_s$ should be 3304 N·m/s and 140 Hz, respectively. It can be seen that the theoretical analysis is basically consistent with the actual response shown in Fig. 12(a)–(c).

Fig. 12(d)–(f) and (g)–(i) shows the experimental results of the proposed servo control structure without and with saturation values of T_s and $\dot{T}_s$, respectively. From Fig. 12(e), the presence of the transmission torque loop makes the amplitude not large, about 3.76 N·m. The electromagnetic torque shows a qualitatively similar behavior with transmission torque, but settles at 4.77 N·m because it must also provide the torque to accelerate the inertial mass of the drive side. From Fig. 12(f), the transmission jerk reaches -100 N·m/s. From Fig. 12(g)–(i), T_s reaches its saturation value ±3 N·m before the motor position reaches the reference position. When the system reaches the reference position, T_e and T_s tend to zero. As can be seen in Fig. 12(i), $\dot{T}_s$ and $\dot{T}_{so}$ reach a saturation value of -40 N·m/s in the reverse direction. In addition, the experimental response of this group lags slightly behind Fig. 12(d)–(f) due to the application of the limiting control of the transmission torque and jerk. Furthermore, the novel servo control structure studied in this article exhibits a certain level of disturbance resistance. When compared to the traditional servo control structure under the premise of basic consistency in position response, the studied servo control structure generates a more severe position drop but with a shorter recovery time after loading.

Fig. 13 shows the results of the proposed servo control structure for different load inertia. The saturation values of T_s and $\dot{T}_s$ are set to ±2 N·m and $\pm$ 30 N·m/s, respectively, and the load torque is 15% of the rated torque. Comparing Fig. 13(a)–(c) and (d)–(f), as the load inertia increases, the system response slows down, and the transmission jerk does not reach saturation. However, the uncertainty in system parameters does not affect the system's steady-state tracking accuracy. Therefore, the control loop design presented in this article exhibits strong robustness in the face of parameter uncertainties.

In addition, experiments are conducted under the planned S-ramp position reference, considering limitations on motor speed, acceleration, and jerk. The comparative results between the conventional servo structure and the proposed control structure are illustrated in Fig. 14(a)–(d) and (e)–(h), respectively. In the proposed control structure, the saturation values for T_s and $\dot{T}_s$ are set to ±1 N·m and ±10 N·m/s, respectively. Compared to the step position reference, the S-ramp position reference, due to the imposed limitations on motor speed, acceleration, and jerk, results in a slower system response with a significant reduction in T_s and $\dot{T}_s$.

From Fig. 14(a)–(d), it can be observed that the motor's position tracking response is fast, resulting in the maximum motor speed exceeding 80 rad/s. Similarly, the response speed of T_s and $\dot{T}_s$ is fast, meeting the requirements of traditional servo control. Although the S-ramp position reference can reduce the magnitude of torque, it still fails to achieve smooth torque

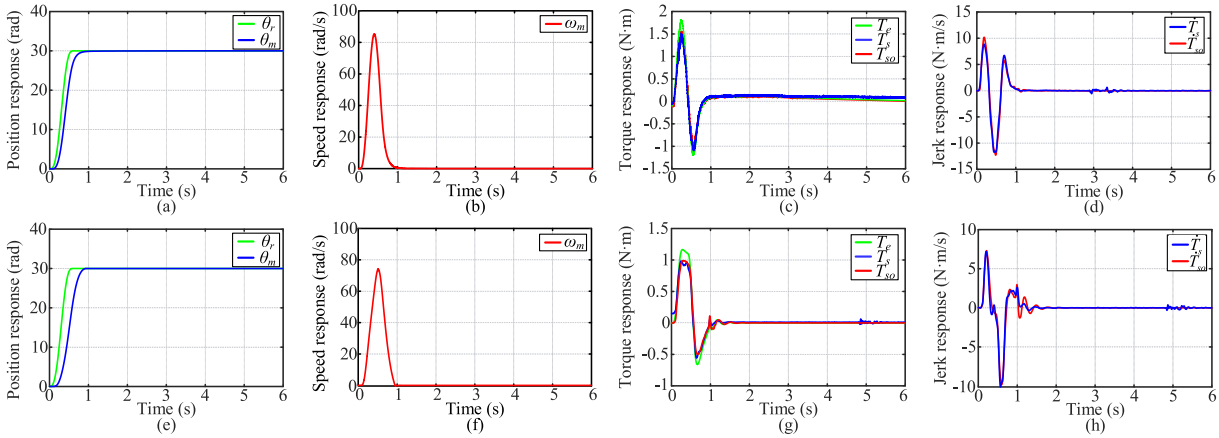

Fig. 14. Experimental comparison results under S-ramp position reference. (a)–(d) Conventional servo control structure. (e)–(h) Control structure with saturation values set at ±1 N·m for transmission torque and ±10 N·m/s for transmission jerk.

control. Furthermore, achieving precise torque tracking requires planning an appropriate position reference signal, which demands considerable expertise and time.

However, as shown in Fig. 14(e)–(h), the motor's position tracking response slows down significantly, with the maximum motor speed less than 80 rad/s. The proposed servo structure successfully constrains T_s and $\dot{T}_s$ within the saturation values, achieving smooth torque control. The torque tracking accuracy can be easily satisfied by simple saturation value settings. Nevertheless, the slight delay in position tracking is precisely because of the novel servo structure sacrificing a certain degree of rapidity of position tracking to pursue smoothness and accuracy of torque tracking.

In summary, the traditional servo control structure cannot ensure the smoothness of transmission states and faces challenges in achieving accurate torque tracking and safety control. However, the control structure proposed in this article can achieve arbitrary limiting control of the transmission torque and its jerk under different load torques and different load inertia, thereby ensuring the transmission smoothness, safety, and accuracy of the robotic joint servo system.

VI. Conclusion

In this article, the transmission characteristics of the joint servo system is analyzed, and a limiting control scheme for the transmission states is proposed. The analysis of the operating characteristics of the transmission states shows that during the dynamic operation of the system, the transmission torque and jerk exhibit oscillation signals, which are related to inertia ratio and oscillation frequency of the system. In particular, both states can change drastically during the motor start-up or sudden load phases, so limiting control is required. Instead of the traditional servo control structure, this article proposes a novel cascade servo control structure consisting of position, transmission torque and jerk. The controller parameters of the three loops are designed by the evaluation function method and the frequency domain method. The operating characteristics and limiting control performance of the transmission states are verified, thus ensuring the transmission accuracy and safety of the flexible joint servo system.

Future work will focus on the analysis of loading performance for the studied servo control structure, and explore effective methods for load compensation.

References

[1] T. Vajsz and L. Számel, "Improved modified DTC-SVM methods for increasing the overload-capability of permanent magnet synchronous motor servo- and robot drives–Part 1," *Periodica Polytechnica Elect. Eng. Comput. Sci.*, vol. 62, no. 3, pp. 65–73, 2018.

[2] J. Li et al., "An iterative parameter tuning method for robot joint motor's sliding mode controller," in *Proc. Chin. Intell. Automat. Conf.*, 2019, pp. 629–637.

[3] T. Li et al., "Calculation of the meshing point position of cycloidal-pin wheel drive for RV reducer in robot," in *Proc. 6th Int. Conf. Meas., Instrum. Automat.*, 2017, pp. 411–415.

[4] D. Huang, P. Zong, and J. Gu, "Defect elimination in torsional harmonic reducer based on harmonic resonance," *Vibroengineering Procedia*, vol. 28, no. 7, pp. 6–11, 2019.

[5] K. Yang et al., "A new methodology for joint stiffness identification of heavy duty industrial robots with the counterbalancing system," *Robot. Comput.-Integr. Manuf.*, vol. 53, pp. 58–71, 2018.

[6] M. Ruderman and M. Iwasaki, "Sensorless torsion control of elastic-joint robots with hysteresis and friction," *IEEE Trans. Ind. Electron.*, vol. 63, no. 3, pp. 1889–1899, Mar. 2016.

[7] V. Stojanovic and D. Prsic, "Robust identification for fault detection in the presence of non-Gaussian noises: Application to hydraulic servo drives," *Nonlinear Dyn.*, vol. 100, no. 4, pp. 2329–2313, 2020.

[8] K. Rani and N. Kumar, "Intelligent controller for hybrid force and position control of robot manipulators using RBF neural network," *Int. J. Dyn. Control*, vol. 7, no. 2, pp. 767–775, 2019.

[9] P. Yang et al., "High-precision rotor position estimation for high-speed SPMSM drive based on state observer and harmonic elimination," in *Proc. Int. Power Electron. Conf.*, 2018, pp. 1966–1971.

[10] S. Haddadin, A. D. Luca, and A. Albu-Schäffer, "Robot collisions: A survey on detection, isolation, and identification," *IEEE Trans. Robot.*, vol. 33, no. 6, pp. 1292–1312, Dec. 2017.

[11] D. Zhi, Z. Feng, W. Xu, R. Kang, and L. Chen, "Design and control of a variable viscous damping actuator (VVDA) for compliant robotic joints," in *Proc. IEEE Int. Conf. Robot. Biomimetics*, 2018, pp. 1876–1881.

[12] Z. Sun et al., "Online suppression of mechanical resonance using extremum seeking control," in *Proc. 37th Chin. Control Conf.*, 2018, pp. 3847–3852.

[13] L. Xiong, P. Shang, S. Feng, L. Yu, and W. Cheng, "Exact limit pressure of high-speed couplings of micro gas turbines for interference fits," in *Proc. IEEE Int. Conf. Mechatron. Automat.*, 2016, pp. 193–198.

[14] S. Kim, "Moment of inertia and friction torque coefficient identification in a servo drive system," *IEEE Trans. Ind. Electron.*, vol. 66, no. 1, pp. 60–70, Jan. 2019.
[15] S. E. Lyshevski, "Control of high-precision direct-drive mechatronic servos: Tracking control with adaptive friction estimation and compensation," *Mechatronics*, vol. 43, pp. 1–5, 2017.
[16] T. Sakuma et al., "Modeling and resonance suppression control for electro-hydrostatic actuator as a two-mass resonant system," *Adv. Robot.*, vol. 32, no. 1, pp. 1–11, 2017.
[17] M. Joost, W. Holzke, C. Mehler, and B. Orlik, "Observer based stress reducing control of elastically coupled multi-mass systems," in *Proc. 13th Int. Conf. IEEE Optim. Elect. Electron. Equip.*, 2012, pp. 1093–1099.
[18] A. A. Radionov, V. Gasiyarov, and V. Khramshin, "Implementation of telemetric on-line monitoring system of elastic torque of rolling mill line of shafting," in *Proc. 2nd Int. Ural Conf. Meas.*, 2017, pp. 450–455.
[19] A. Arkkio, S. Cederstrom, H. A. A. Awan, S. E. Saarakkala, and T. P. Holopainen, "Additional losses of electrical machines under torsional vibration," *IEEE Trans. Energy Convers.*, vol. 33, no. 1, pp. 245–251, Mar. 2018.
[20] A. A. Ahmed, B. K. Koh, and Y. I. Lee, "A comparison of finite control set and continuous control set model predictive control schemes for speed control of induction motors," *IEEE Trans. Ind. Inform.*, vol. 14, no. 4, pp. 1334–1346, Apr. 2018.
[21] C. Wang, M. Yang, W. Zheng, J. Long, and D. Xu, "Vibration suppression with shaft torque limitation using explicit MPC-PI switching control in elastic drive systems," *IEEE Trans. Ind. Electron.*, vol. 62, no. 11, pp. 6855–6867, Nov. 2015.
[22] P. Serkies and K. Szabat, "Estimation of the state variables of the two-mass system using fuzzy Kalman filter," in *Proc. IEEE Int. Symp. Ind. Electron.*, 2013, pp. 1–6.
[23] X. Liu, F. Zhao, S. S. Ge, Y. Wu, and X. Mei, "End-effector force estimation for flexible-joint robots with global friction approximation using neural networks," *IEEE Trans. Ind. Inform.*, vol. 15, no. 3, pp. 1730–1741, Mar. 2019.
[24] P. Serkies, T. Orlowska-Kowalska, M. Cychowski, and K. Szabat, "Robust model predictive speed control of the drive system with an elastic joint," in *Proc. IEEE Eurocon-Int. Conf. Comput. Tool*, 2011, pp. 1–4.
[25] M. Cychowski, K. Szabat, and T. Orlowska-Kowalska, "Constrained model predictive control of the drive system with mechanical elasticity," *IEEE Trans. Ind. Electron.*, vol. 56, no. 6, pp. 1963–1973, Jun. 2009.
[26] H. Bolouri Novin and H. Ghadiri, "Particle swarm optimization base explicit model predictive controller for limiting shaft torque," in *Proc. 5th Iranian Joint Congr. Fuzzy Intell. Syst.*, 2017, pp. 35–40.
[27] P. Serkies and K. Szabat, "Predictive position control of a two-mass system with an induction motor in a wide range of speed changes," in *Proc. Adv. Control Elect. Drives Power Electron. Converters*, 2017, pp. 53–74.
[28] P. Serkies and K. Szabat, "Effective damping of the torsional vibrations of the drive system with an elastic joint based on the forced dynamic control algorithms," *J. Vib. Control*, vol. 25, no. 16, pp. 2225–2236, 2019.
[29] M. Joost, C. Mehler, and B. Orlik, "Dynamic load change stress minimizing control of elastically coupled multi-mass systems," in *Proc. 12th Int. Conf. Optim. Elect. Electron. Equip.*, 2010, pp. 754–759.
[30] E. A. Maklakova, S. S. Voronin, V. R. Gasiyarov, and A. S. Maklakov, "The dynamic torque decrease of the rolling stand electric drive for metal biting," in *Proc. IEEE Conf. Russian Young Researchers Elect. Electron. Eng.*, 2017, pp. 939–942.
[31] K. Szabat, T. Tran-Van, and M. Kamiński, "A modified fuzzy luenberger observer for a two-mass drive system," *IEEE Trans. Ind. Inform.*, vol. 11, no. 2, pp. 531–539, Apr. 2015.
[32] G. Zhang, "Speed control of a two-inertia system by PI/PID control," *IEEE Trans. Ind. Electron.*, vol. 47, no. 3, pp. 603–609, Jun. 2000.

Can Wang received the B.S. degree in electrical engineering from Harbin University of Science and Technology, Harbin, China, in 2012, and the M.S. and Ph.D. degrees in power electronics and electrical drives from Harbin Institute of Technology, Harbin, China, in 2014 and 2019, respectively.

In 2019, she was with the College of Mechatronics and Control Engineering, Shenzhen University as an Assistant Professor. She has authored more than 20 technical papers published in journals and conference proceedings. Her current research interests include PMSM servo system and two-mass system control.

Yongquan Zhuang received the B.S. degree in automation from Wuyi University, Nanping, China, in 2022. He is currently working toward the master's degree in control engineering with the College of Mechatronics and Control Engineering, Shenzhen University, Shenzhen, China.

His current research interests include PMSM servo system, two-mass system control, and transmission torque loop control algorithm.

Jinling Yang received the B.S. degree in electrical engineering and automation from Beijing Institute of Technology, Zhuhai, China, in 2019, and the M.S. degree in electronic information from the College of Mechatronics and Control Engineering, Shenzhen University, Shenzhen, China, in 2023.

His current research interest includes the servo motor drive and control.

Yuchao Liu received the M.S. and Ph.D. degrees in electrical engineering from Harbin Institute of Technology, Harbin, China, in 2014 and 2019, respectively.

From 2017 to 2018, she was a visiting student with Imperial College London, U.K. From 2019 to 2022, she was a Lecturer with Harbin Engineering University, Harbin, China and then a Research Fellow with the Power Electronics, Machines Control Research Group, University of Nottingham, Nottingham, U.K. Since 2023, she has been a Lecturer with Northumbria University, Newcastle upon Tyne, U.K. Her research interests include high-power converters, motor drives, multiterminal dc transmission, integration of renewable energy, power management of microgrids, and power electronics for enabling the electrification of transportation.

Jianfei Pan (Member, IEEE) received the Ph.D. degree in electrical engineering from the Department of Electrical Engineering, The Hong Kong Polytechnic University, Hong Kong, in 2006.

He is currently with the College of Mechatronics and Control Engineering, Shenzhen University, Shenzhen, China. His main research interest includes the design and control of linear motors and generators.